

THE *Gaia*-ESO SURVEY: METAL-RICH BANANAS IN THE BULGE

ANGUS A. WILLIAMS¹, N. W. EVANS¹, MATTHEW MOLLOY², GEORGES KORDOPATIS³, M. C. SMITH⁴, J. SHEN⁴, G. GILMORE¹, S. RANDICH⁵, T. BENSBY⁶, P. FRANCOIS⁷, S. E KOPOSOV¹, A. RECIO-BLANCO⁸, A. BAYO⁹, G. CARRARO¹⁰, A. CASEY¹, T. COSTADO¹¹, E. FRANCIOSINI⁵, A. HOURIHANE¹, P. DE LAVERNY⁸, J. LEWIS¹, K. LIND¹², L. MAGRINI⁵, L. MONACO¹³, L. MORBIDELLI⁵, G. G SACCO⁵, C. WORLEY¹, S. ZAGGIA¹⁴, AND Š. MIKOLAITIS¹⁵

¹ Institute of Astronomy, Madingley Road, Cambridge CB3 0HA, UK; aamw3@ast.cam.ac.uk, nwe@ast.cam.ac.uk

² Kavli Institute for Astronomy & Astrophysics, Peking University, Beijing 100871, China

³ Leibniz-Institut für Astrophysik Potsdam, An der Sternwarte 16, D-14482 Potsdam, Germany

⁴ Key Laboratory for Research in Galaxies and Cosmology, Shanghai Astronomical Observatory, Chinese Academy of Sciences, 80 Nandan Road, Shanghai 200030, China

⁵ INAF Osservatorio Astrofisico di Arcetri, Largo E. Fermi 5, I-50125 Florence, Italy

⁶ Lund Observatory, Dept of Astronomy and Theoretical Physics, Box 43, SE-221 00 Lund, Sweden

⁷ GEPI, Observatoire de Paris, CNRS, Université Paris Diderot, 5 Place Jules Janssen, F-92190 Meudon, France

⁸ Laboratoire Lagrange, Université Côte d'Azur, Observatoire de la Côte d'Azur, CNRS, Bvd. de l'Observatoire, CS 34229, F-06340 Nice, France

⁹ Instituto de Física y Astronomía, Universidad de Valparaíso, Valparaíso, Chile

¹⁰ European Southern Observatory, Alonso de Cordova 3107, Vitacura, Santiago de Chile, Chile

¹¹ Instituto de Astrofísica de Andalucía-CSIC, Apdo. 3004, E-18080 Granada, Spain

¹² Max-Planck Institut für Astronomie, Königstuhl 17, D-69117 Heidelberg, Germany

¹³ Departamento de Ciencias Físicas, Universidad Andres Bello, Republica 220, Santiago, Chile

¹⁴ INAF—Padova Observatory, Vicolo dell'Osservatorio 5, I-35122 Padova, Italy

¹⁵ Institute of Theoretical Physics and Astronomy, Vilnius University, Saulėtekio al. 3, LT-10222, Vilnius, Lithuania

Received 2016 April 1; revised 2016 May 27; accepted 2016 May 30; published 2016 June 21

ABSTRACT

We analyze the kinematics of ~ 2000 giant stars in the direction of the Galactic bulge, extracted from the *Gaia*-ESO survey in the region $-10^\circ \lesssim \ell \lesssim 10^\circ$ and $-11^\circ \lesssim b \lesssim -3^\circ$. We find distinct kinematic trends in the metal-rich ($[M/H] > 0$) and metal-poor ($[M/H] < 0$) stars in the data. The velocity dispersion of the metal-rich stars drops steeply with latitude, compared to a flat profile in the metal-poor stars, as has been seen previously. We argue that the metal-rich stars in this region are mostly on orbits that support the boxy-peanut shape of the bulge, which naturally explains the drop in their velocity dispersion profile with latitude. The metal-rich stars also exhibit peaky features in their line of sight velocity histograms, particularly along the minor axis of the bulge. We propose that these features are due to stars on resonant orbits supporting the boxy-peanut bulge. This conjecture is strengthened through the comparison of the minor axis data with the velocity histograms of resonant orbits generated in simulations of buckled bars. The “banana” or 2:1:2 orbits provide strongly bimodal histograms with narrow velocity peaks that resemble the *Gaia*-ESO metal-rich data.

Key words: galaxies: general – galaxies: kinematics and dynamics – Galaxy: bulge

1. INTRODUCTION

The metallicity and velocity distributions change across the Galactic Bulge, as the chemical history and orbital content varies from field to field (e.g., Babusiaux 2016). One of the aims of the large-scale spectroscopic surveys (such as ARGOS, APOGEE, and *Gaia*-ESO) is to map out the correlations between metallicity and kinematics (e.g., Ness et al. 2013; Rojas-Arriagada et al. 2014; Ness et al. 2016). This offers the promise of uncovering the history of the Bulge, as well as its present-day structure.

Bars are largely built from orbits trapped around the main prograde periodic orbits aligned with the long axis. These nearly planar orbits can become vertically unstable and sire families librating around the vertical resonances (e.g., Pfenniger & Friedli 1991). They are called the “banana” or “pretzel” orbits because of their characteristic morphology (Miralda-Escude & Schwarzschild 1989; Portail et al. 2015). It has long been suspected that they support the boxy or peanut-shaped bulges seen in external galaxies. The discovery of the bimodal distribution in red clump magnitudes on minor axis fields (McWilliam & Zoccali 2010; Nataf et al. 2010) seemed to provide evidence for the existence of resonant orbits in the Galactic Bulge itself (e.g., Portail et al. 2015).

In this Letter, we examine the bulge fields in the fourth data release of the *Gaia*-ESO survey in Section 2. We identify narrow features in the metallicity and velocity distributions as the signature of resonant orbits (Section 3) and provide a comparison with the expected properties of resonant orbits from simulations (Section 4). This is suggestive of the presence of substantial numbers of banana orbits in the bar, predominantly populated by the metal-rich stars.

2. DATA

Gaia-ESO is a public spectroscopic survey, providing high-quality spectra for $\sim 10^5$ stars in the Milky Way (Gilmore et al. 2012). Spectra are taken using the VLT-FLAMES instrument. Here, we analyze a subset of 1938 of these stars located in the direction of the Galactic bulge, taken from the 4th internal data release (iDR4). We make a metallicity cut, $-1.7 \leq [M/H] \leq 1$, and a surface gravity cut, $\log g < 3.5$, to ensure that we have a clean sample of giants. Our specific flag cuts are: `GES_FLD == “Bulge”` and `GES_TYPE == “GE_MW_BL.”` Typical uncertainty in line of sight velocity (metallicity) is ~ 0.4 km s^{−1} (~ 0.1 dex).

Figure 1 depicts the distribution of the *Gaia*-ESO bulge sample (including our cuts) in longitude and latitude, and

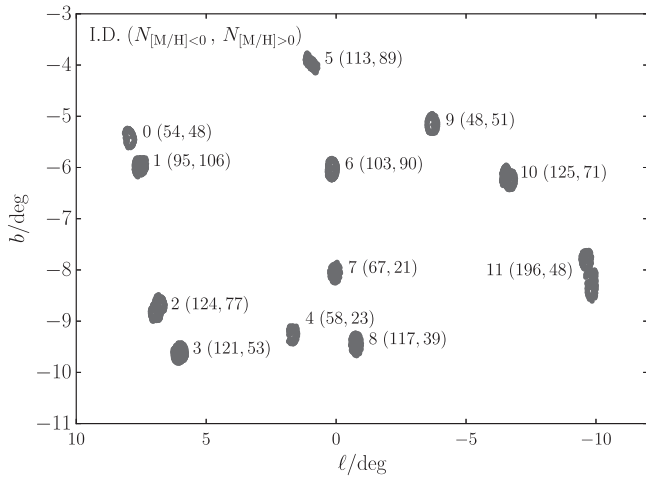


Figure 1. Distribution of our sample in Galactic longitude and latitude. Each field is labeled by its ID number, followed in brackets by the number of stars with $[M/H] < 0$ and the number with $[M/H] > 0$.

Figure 2 depicts the selection in color and magnitude with the combined VVV photometry for all the fields underlaid. The sample from iDR4 covers a larger area on the sky than previous data releases (see, e.g., Rojas-Arriagada et al. 2014), giving us more scope to constrain trends with on-sky position. Each of our fields contains between 80 and 250 stars. The *Gaia*-ESO bulge selection consists of a color cut in each field of $(J - K)_0 > 0.38$, which is then reddened appropriately given the extinction in that direction, and a magnitude cut $12.9 < J_0 < 14.1$, which is also modified in some fields to allow both red clump populations to be represented in the sample (for more details, see Rojas-Arriagada et al. 2014).

3. KINEMATICS AS A FUNCTION OF METALLICITY

Based on the clearly bimodal structure of our sample in the $[\alpha/M]$ - $[M/H]$ plane, shown in Figure 3, we split the sample by metallicity. We dub stars with $[M/H] > 0$ as “metal-rich” and stars with $[M/H] < 0$ as “metal-poor.” This gives a sample of 1222 metal-poor stars and 716 metal-rich stars. The metal-poor sample is also α -rich, whereas the metal-rich sample is more disk-like (α -poor). We then separately analyze the kinematics of each of these samples across our 12 fields. We correct for solar motion using a local circular speed of 240 km s^{-1} and solar reflex motion of $(11.1, 12.24, 7.25) \text{ km s}^{-1}$ (Schönrich et al. 2010).

The *Gaia*-ESO sample exhibits features that have been observed in other studies (for a summary, see Babusiaux 2016). Figure 4 shows the strong correlation between mean line of sight velocity and Galactic longitude, indicative of rotation. Here, we find no discernible difference between the rotational signature in the metal-rich stars and the metal-poor stars, both of which show a velocity gradient of $\sim 8 \text{ km s}^{-1} \text{ deg}^{-1}$. The dispersion and shape of the line of sight velocity distributions of each population, however, show marked differences. Figure 5 depicts the line of sight velocity dispersion of the stars as a function of latitude. The metal-rich stars exhibit a steep decline in velocity dispersion with latitude. A simple linear fit gives a gradient of $7.4 \pm 0.7 \text{ km s}^{-1} \text{ deg}^{-1}$. The metal-poor stars, on the other hand, present a much flatter dispersion profile, with slope $2.0 \pm 1.0 \text{ km s}^{-1} \text{ deg}^{-1}$. This property has been seen in other surveys (see Figure 4 of

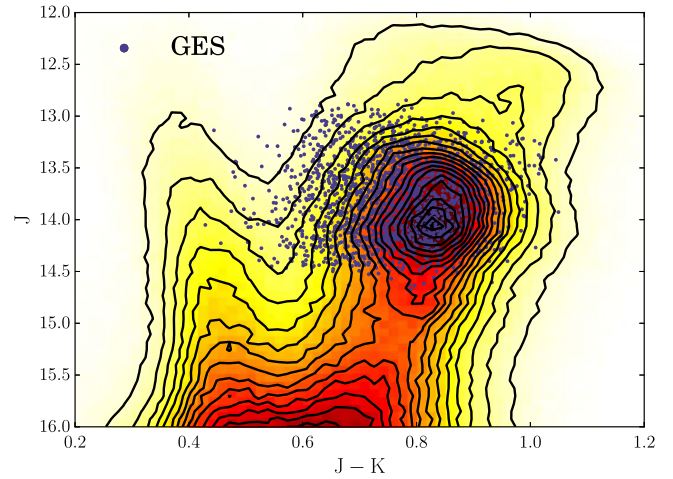


Figure 2. Selection of the *Gaia*-ESO bulge targets in color and magnitude. The contours are of the combined VVV photometry from all of the fields, and the purple points represent our sample.

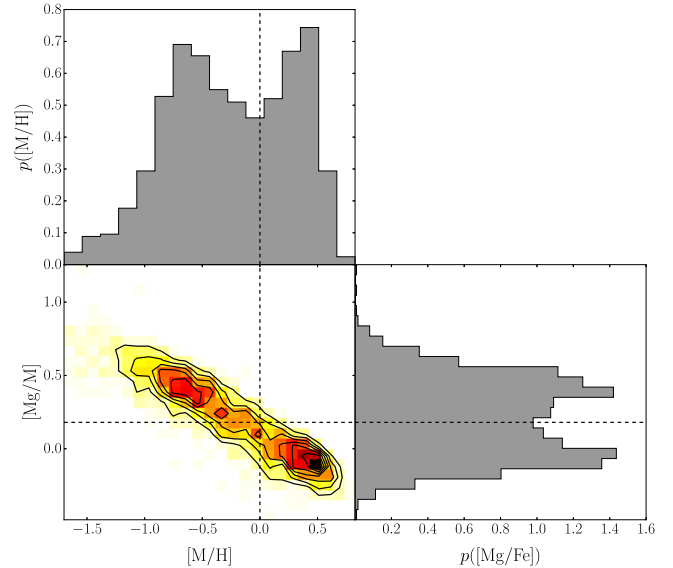


Figure 3. $[Mg/M]$ - $[M/H]$ distribution of our sample. One can clearly see two overdensities in this plane, which are reflected in the two marginalized distributions. We split the sample around $[M/H] = 0$, which effectively also splits in $[Mg/M]$. The low-metallicity population has higher α -element enrichment, whereas the high-metallicity population resembles the disk.

Babusiaux 2016) and has been shown to be consistent with specific numerical simulations (e.g., Babusiaux et al. 2010). The evident separation in both chemistry and kinematics is suggestive that the two sequences have different formation histories. We might also expect interesting or unusual features in the line of sight velocity distributions. For example, Nidever et al. (2012) first detected cold, high-velocity peaks in the APOGEE bulge fields near the Galactic plane, and Molloy et al. (2015a) subsequently proposed that these structures were a consequence of stars on resonant orbits in the bar (see also Debattista et al. 2015 for a related idea).

Further examples of this type of phenomenon, now only in the velocity distributions of the *Gaia*-ESO metal-rich sample, are shown in the two leftmost panels of Figure 6. Fields 5 (Baade’s window) and 6 are of particular interest because they lie along the minor axis of the bar, where the X-shape is observed (e.g., Gonzalez et al. 2015). They are also close

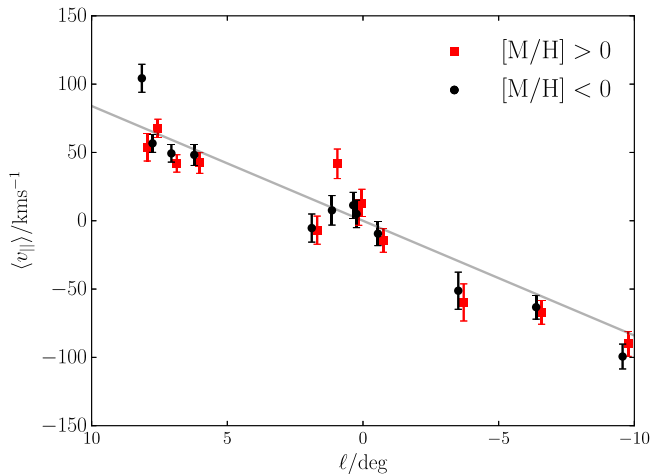


Figure 4. Mean line of sight velocities as a function of longitude. At each longitude, the red squares (metal-rich) and black circles (metal-poor) are slightly offset from one another for clarity. Both the metal-rich and metal-poor samples exhibit the usual rotational signature seen in bulge stars. The line is a linear fit to the data with gradient $8.4 \text{ km s}^{-1} \text{ deg}^{-1}$. The metal-rich and metal-poor rotation curves are both consistent with this value at a 1σ level.

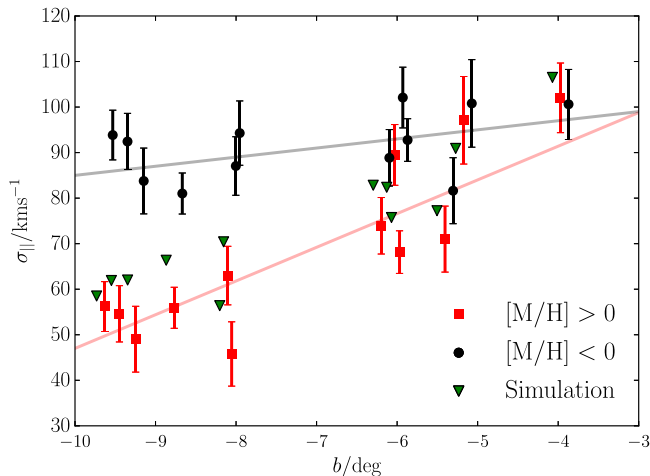


Figure 5. Line of sight velocity dispersion as a function of latitude. At each latitude, the red squares (metal-rich), black circles (metal-poor), and green triangles (simulation) are slightly offset from one another for clarity. The metal-rich stars in our sample become significantly colder as $|b|$ increases, whereas the metal-poor stars are consistent with being one temperature. The two lines are simple linear fits to the data. The metal-poor stars have a velocity dispersion gradient of $2.0 \pm 1.0 \text{ km s}^{-1} \text{ deg}^{-1}$, whereas the metal-rich stars have a gradient of $7.4 \pm 0.7 \text{ km s}^{-1} \text{ deg}^{-1}$. The green triangles show the velocity dispersion extracted from the simulation.

enough to the Galactic plane that the density of the boxy-peanut bulge is still relatively high, so the proportion of metal-rich stars is favorable compared to other minor axis fields at higher latitudes. The velocity distributions for these fields are multimodal, with narrow peaks at non-zero line of sight velocities. At field 5 (Baade’s Window), there are three narrow peaks; at field 6, there are two broader peaks separated by a small valley. Such features are present in other fields and are particularly prominent at $\ell \sim 0^\circ$, along the short axis of the bar.

4. RESONANT ORBITS IN THE BULGE

Orbits in the Galaxy are usually characterized in terms of three frequencies, κ , Ω , and ν , describing oscillations in the radial, azimuthal, and vertical directions, respectively. The bar

rotates at a pattern speed Ω_b , and this perturbation creates resonant orbits that satisfy

$$m\kappa = n(\Omega - \Omega_b), \quad (1)$$

where m and n are integers. The quantity $\Omega - \Omega_b$ is the azimuthal frequency of the resonance in the frame that corotates with the bar and, since $\Omega - \Omega_b$ is commensurate with κ , a resonant orbit will be closed in the corotating frame (see, e.g., Molloy et al. 2015b). Simulations of barred spirals as well as studies of analytic gravitational potentials confirm that the morphology of the bar is largely supported by stars librating around these resonances (e.g., Molloy et al. 2015a). The 2:1 resonance (two radial oscillations per revolution) sires one of the most important families supporting the backbone of any bar. Resonances also exist in which the vertical frequency becomes commensurate with κ and $\Omega - \Omega_b$. “Banana,” or 2:1:2, orbits are examples of this kind of resonance in which there are also two vertical oscillations per revolution, as shown in Figure 7.

Here, we will use the sample of resonant orbits extracted by the method of Molloy et al. (2015b) from a simulation of Shen et al. (2010). The bar is formed from $m = 2$ instabilities in a massive disk that subsequently become unstable to buckling (e.g., Raha et al. 1991). The endpoint of the simulation is a boxy bulge with a pattern speed of $\sim 40 \text{ km s}^{-1} \text{ kpc}^{-1}$ (Shen & Li 2016). When viewed at an angle of 15° , the model fits the mean motion and velocity dispersion data on the minor axis ($b = 0^\circ$), as well as a sequence of longitudinal fields for $b = -4^\circ$ and $b = -6^\circ$ (see Figure 4 of Shen et al. 2010 for more details). We show as green triangles in Figure 5 the velocity dispersion of the simulation particles in the *Gaia*-ESO fields as a function of latitude. The simulation matches the behavior of the velocity dispersion of the metal-rich stars. Although we cannot reasonably expect this simulation to be a highly accurate match to the inner Milky Way, its structural properties and gross kinematics are broadly correct.

There is substantial degeneracy in the way in which different orbits can be superposed to make a triaxial bar model. The simulation is a useful tool for understanding which types of orbit are likely populated, but we do not expect the relative proportion of these orbits to be correct for the Milky Way bar. If the data set were much larger, we could perform Schwarzschild modeling: the relative weights of the orbital families extracted from the simulation would be fitting parameters. However, since the data are sparse, it is unrealistic to expect to constrain quantitatively the actual proportions of the different families. Our study is less ambitious: we seek to find signs in the data that are suggestive of specific orbital families being highly populated. Using the method of Molloy et al. (2015b), we extract the periodic orbits lying on the 2:1, 3:1 and 5:2 in-plane resonances from the simulation by requiring $(\Omega - \Omega_b)/\kappa$ to equal m/n within some tolerance $\epsilon = 0.1$. A heliocentric distance cut of $6.8 < D/\text{kpc} < 14$ has been applied to the simulation data. The distance selection function of *Gaia*-ESO is much more complicated in reality, but this is a simple and plausible cut to use when comparing the simulations to the data. Finally, we also extract the banana orbits from the 2:1 sample with the additional cut $0.9 < \nu/\kappa < 1.1$. The velocity histograms provided by these orbital families in *Gaia*-ESO fields 5 and 6 are shown in Figure 6. Field 5 (Baade’s window) is relatively well sampled because of the low reddening. The

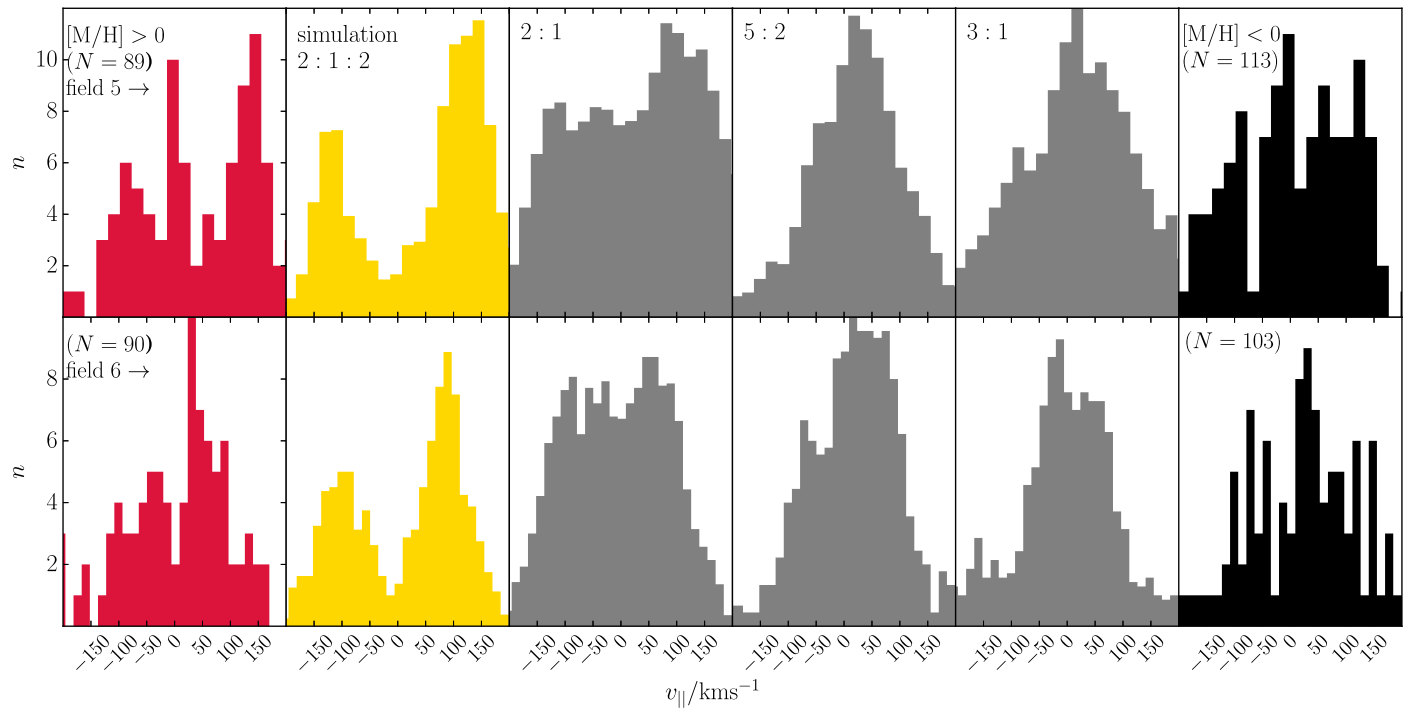


Figure 6. Line of sight velocity distributions of stars in field 5 (Baade’s window) and field 6. The red (black) filled histograms represent the metal-rich (metal-poor) stars. The velocity histograms of some of the dominant resonant orbits from the simulation of Shen et al. (2010) extracted by the method of Molloy et al. (2015b) are shown in the remaining panels, with the “banana” orbits shown in filled yellow. The same bins are used in each row of histograms. There is a striking resemblance between the velocity peaks in the metal-rich stars and those produced by the 2:1:2 resonance. The metal-poor stars do not appear to possess the same structure.

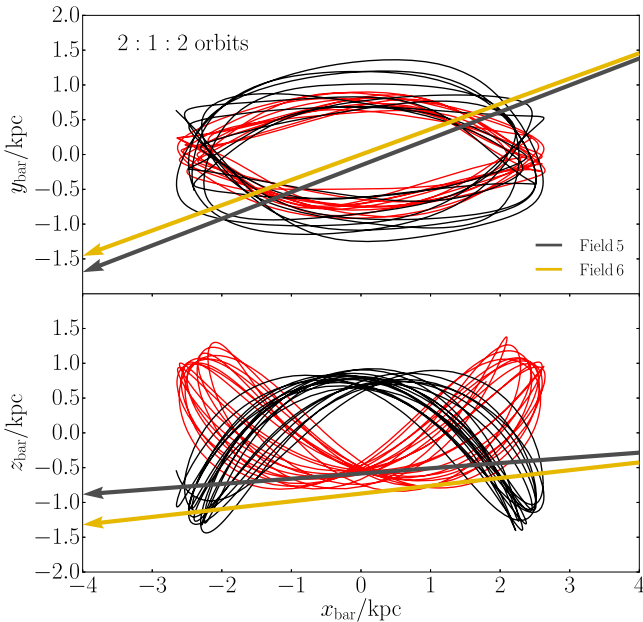


Figure 7. Two orbits closely librating around the 2:1:2 resonance in the frame of the bar extracted from the simulation of (Shen et al. 2010). The “banana” shape is clear in the x - z projection. Overplotted are two arrows representing approximate line of sight directions for fields 5 (Baade’s window, gray) and 6 (gold).

high-velocity peaks in the data resemble banana orbits moving toward us (predominantly on the near-side, $v_{\parallel} \sim -90 \text{ km s}^{-1}$) and away from us (far-side, $v_{\parallel} \sim 140 \text{ km s}^{-1}$). There is also a narrow peak in the data at $v_{\parallel} \approx 0$, which is likely a combination of disk contamination and other resonances (e.g., 5:2 and 3:1). In field 6, there are possible peaks at

$\sim \pm 40 \text{ km s}^{-1}$. Finally, we note a possibly related result—a very narrow velocity minimum on the Bulge minor axis was also reported in red clump stars in Appendix A of Ness et al. (2012).

If the multimodal structure of the velocity histogram of metal-rich stars in Baade’s Window is due to banana orbits, then we would expect to see their signature in other well-sampled minor axis fields. The second row of Figure 6 shows this is possibly the case. Field 6 is centered on ($\ell = 0^\circ 16, b = -6^\circ 03$). The bimodality of the velocity histogram data is also matched in the velocity distribution of the banana orbits. There is, however, a discrepancy in the location of the velocities of the two peaks. This, however, is controlled by the curvature of the banana orbits and so may be adjusted by changing the potential of the bar. In the other minor axis *Gaia*-ESO fields, the bar density has dropped significantly, and with it the number of metal-rich stars in each field. This leads to noisier histograms.

Since we are dealing with relatively few stars, assessment of the significance of the peaks in the data is necessary. We fitted Gaussian mixture models to the velocity distributions in fields 5 and 6 using the SCIKIT-LEARN module for PYTHON (Pedregosa et al. 2012). We then approximated the evidence for a given number of Gaussian components using the Bayesian information criterion (BIC). The BIC offsets changes in the maximum likelihood for a given number of Gaussians by a penalty factor for introducing more parameters. For the metal-poor stars, only one Gaussian component is favored in fields 5 and 6, which is consistent with the hypothesis that they belong to a dynamically simpler spheroid. For the metal-rich stars, we found that two components were favored in field 5 (Baade’s window), so that the central peak and leftmost peak in the data are combined into a single Gaussian and the rightmost peak is

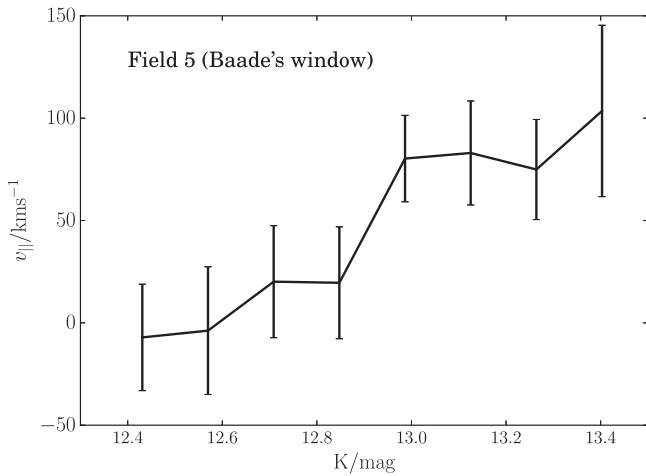


Figure 8. Mean line of sight velocity of stars in field 5 (Baade’s window) as a function of K-band magnitude. One can see evidence for a correlation between K, a rough proxy for distance, and the mean line of sight velocity. The stars that are on the far side of the bulge have larger line of sight velocities. This is qualitatively compatible with the simulation, which predicts a positive correlation between $v_{||}$ and line of sight distance. Though the signal is noticeable here, we do not see an equivalent signal in field 6.

the second Gaussian. In field 6, the BIC informs us that only one Gaussian component is necessary before overfitting the metal-rich velocity data. According to this particular method, then, the evidence for bimodality in field 6 is actually weaker than our eyes might have us believe. Nonetheless, we believe that taken together the velocity distributions of these fields are interesting. Furthermore, we would expect some level of disk contamination in both of these fields at around $v_{||} \sim 0$ km s⁻¹, the removal of which could increase the significance of the bimodality. The expected level of foreground disk contamination in the two fields using the Besançon model (Robin et al. 2003) is $\sim 5\%$. In field 5 (Baade’s Window), we find that 11% of stars have $-10 < v_{||}/\text{km s}^{-1} < 10$. Given our estimate of the contamination, a significant fraction of the stars contributing to the central peak in the velocity histogram of metal-rich stars are likely disk stars.

Another intriguing feature in the data is that, in Baade’s window, the line of sight velocity and K-band magnitude are correlated (see Figure 8). This is predicted by the simulation, so that stars in the high-velocity peak are found on the far side of the bar (larger K magnitude). The stars with $v_{||} \sim 0$ km s⁻¹ are generally found at brighter magnitudes, consistent with the picture that they are contaminants from the disk. Interestingly, we do not see the same correlation in field 6.

5. CONCLUSIONS

We compared the velocity histograms of the metal-rich ($[M/H] > 0$) stars in the *Gaia*-ESO fields on the minor axis of the Galactic bulge with those produced by the most populated resonant orbits in an *N*-body simulation of a buckled bar. The narrow peaks that are seen in the data resemble those produced by the “banana” or 2:1:2 resonant orbits in the simulation. Though these results are intriguing, more statistics are required to confirm the hypothesis that 2:1:2 orbits are heavily populated in the Galactic bar.

This work supplements the earlier kinematic study of Vásquez et al. (2013). Targeting the bright and faint red

clumps at ($\ell = 0^\circ, b = -6^\circ$), very close to our field 6, they found differences in the radial velocity and proper motion distributions consistent with stars in the bright clump moving toward us and in the faint clump moving away. However, they argued that the metal-poor stars are preferentially on elongated orbits and the metal-rich ones on more axisymmetric orbits, contrary both to the results in this paper and theoretical expectation (Babusiaux et al. 2010). Their argument is open to question as it is not based on orbit integrations, but on visual inspection of radial velocity histograms split according to metallicity. Nonetheless, proper motions may indeed offer hope for confirming the structure, as the banana orbits have a characteristic morphology and hence a strong correlation between μ_ℓ , μ_b , and $v_{||}$. The OGLE survey has produced such measurements, and *Gaia* may also provide proper motions for some stars in the bulge.

The weighting of the different resonances tells us about the conditions under which the boxy bulge formed via the buckling instability. Metallicity gradients in the original barred disk will cause stars with different radii and hence metallicities to be mapped onto different vertical resonances. This in principle offers us an opportunity to map out the history of buckling in the inner galaxy, as well as trace back the state of the pristine disk in the epoch before buckling.

Based on data products from observations made with ESO Telescopes at the La Silla Paranal Observatory under programme ID 188.B-3002. These data products have been processed by the Cambridge Astronomy Survey Unit (CASU) at the Institute of Astronomy, University of Cambridge, and by the FLAMES/UVES reduction team at INAF/Osservatorio Astrofisico di Arcetri. These data have been obtained from the *Gaia*-ESO Survey Data Archive, prepared and hosted by the Wide Field Astronomy Unit, Institute for Astronomy, University of Edinburgh, which is funded by the UK Science and Technology Facilities Council. This work was partly supported by the European Union FP7 programme through ERC grant number 320360 and by the Leverhulme Trust through grant RPG-2012-541. We acknowledge the support from INAF and Ministero dell’Istruzione, dell’Università e della Ricerca (MIUR) in the form of the grant “Premiale VLT 2012.” The results presented here benefit from discussions held during the *Gaia*-ESO workshops and conferences supported by the European Science Foundation (ESF) through the GREAT Research Network Programme.

REFERENCES

- Babusiaux, C. 2016, PASA, in press (arXiv:1601.07761)
- Babusiaux, C., Gómez, A., Hill, V., et al. 2010, *A&A*, **519**, A77
- Debatista, V. P., Ness, M., Earp, S. W. F., & Cole, D. R. 2015, *ApJL*, **812**, L16
- Gilmore, G., Randich, S., Asplund, M., et al. 2012, *Msngr*, **147**, 25
- Gonzalez, O. A., Zoccali, M., Debatista, V. P., et al. 2015, *A&A*, **583**, L5
- McWilliam, A., & Zoccali, M. 2010, *ApJ*, **724**, L491
- Miralda-Escude, J., & Schwarzschild, M. 1989, *ApJ*, **339**, 752
- Molloy, M., Smith, M. C., Evans, N. W., & Shen, J. 2015a, *ApJ*, **812**, L46
- Molloy, M., Smith, M. C., Shen, J., & Evans, N. W. 2015b, *ApJ*, **804**, 80
- Nataf, D. M., Udalski, A., Gould, A., Fouqué, P., & Stanek, K. Z. 2010, *ApJL*, **721**, L28
- Ness, M., Freeman, K., Athanassoula, E., et al. 2012, *ApJ*, **756**, 22
- Ness, M., Freeman, K., Athanassoula, E., et al. 2013, *MNRAS*, **432**, 2092
- Ness, M., Zasowski, G., Johnson, J. A., et al. 2016, *ApJ*, **819**, 2
- Nidever, D. L., Zasowski, G., Majewski, S. R., et al. 2012, *ApJL*, **755**, L25
- Pedregosa, F., Varoquaux, G., Gramfort, A., et al. 2012, arXiv:1201.0490
- Pfenniger, D., & Friedli, D. 1991, *A&A*, **252**, 75

- Portail, M., Wegg, C., & Gerhard, O. 2015, [MNRAS](#), **450**, L66
- Raha, N., Sellwood, J. A., James, R. A., & Kahn, F. D. 1991, [Natur](#), **352**, 411
- Robin, A., Reylé, C., Derrière, S., & Picaud, S. 2003, [A&A](#), **409**, 523
- Rojas-Arriagada, A., Recio-Blanco, A., Hill, V., et al. 2014, [A&A](#), **569**, A103
- Schönrich, R., Binney, J., & Dehnen, W. 2010, [MNRAS](#), **403**, 1829
- Shen, J., & Li, Z.-Y. 2016, Galactic Bulges, [418](#), 233
- Shen, J., Rich, R. M., Kormendy, J., et al. 2010, [ApJL](#), **720**, L72
- Vásquez, S., Zoccali, M., Hill, V., et al. 2013, [A&A](#), **555**, A91